

Neural Connectome of the Ctenophore Statocyst

Kei Jokura^{1,2,3,4,5*}, Sanja Jasek^{1,2,6}, Lara Niederhaus⁶, Paweł Burkhardt⁷, Gáspár Jékely^{1,2,6,*}

¹ Living Systems Institute, University of Exeter, Exeter, EX4 4QD, United Kingdom

² Biosciences, Faculty of Health and Life Sciences, University of Exeter, Exeter EX4 4QD, UK

³ Grass Laboratory, Marine Biological Laboratory, Woods Hole, MA 02543, USA

⁴ Exploratory Research Center on Life and Living Systems (ExCELLS), Okazaki, 444-8787, Japan

⁵ National Institute for Basic Biology (NIBB), Okazaki, 444-8585, Japan

⁶ Heidelberg University, Centre for Organismal Studies (COS), 69120 Heidelberg, Germany

⁷ Michael Sars Centre, University of Bergen, Norway



1

* Correspondence: jokura@nibb.ac.jp, gaspar.jekely@cos.uni-heidelberg.de

Abstract

Ctenophores possess a unique gravity receptor (statocyst) in their aboral organ formed by four clusters of ciliated balancer cells that collectively support a statolyth. During reorientation, differential load on the balancer cilia leads to altered beating of the ciliated comb rows to elicit turns. To study the neural bases of gravity sensing, we imaged by volume electron microscopy (vEM) the aboral organ of the ctenophore *Mnemiopsis leidyi*. We reconstructed 972 cells, including syncytial neurons that form a nerve net. The syncytial neurons synapse on the balancer cells and also form reciprocal connection with the bridge cells that span the statocyst. High-speed imaging revealed that balancer cilia beat and arrest in a coordinated manner but with differences between the sagittal and tentacular planes of the animal, reflecting nerve-net organisation. Our results suggest a coordinating rather than sensory-motor function for the nerve net and inform our understanding of the diversity of nervous-system organisation across animals.

Introduction

Ctenophores, or comb jellies, are gelatinous marine animals that actively swim by beating rows of fused cilia known as comb plates. These coordinated ciliary movements not only generate propulsion but also allow precise control of body orientation and directional changes within the water column. Despite lacking a centralized nervous system, ctenophores exhibit sophisticated and dynamic behavioural patterns and respond to a broad range of external stimuli, suggesting the presence of an evolutionarily unique and functionally integrated sensorimotor system coordinating locomotion and posture. Several components of the ctenophore nervous system have been described, including a subepithelial nerve net (SNN), mesogleal neurons, tentacular nerves, and elements of the nervous system in the aboral organ (Hernandez-Nicarce, 1984; Hertwig, 1880; Jager et al., 2010). These neural structures are characterized by unique features such as a syncytial architecture (Burkhardt et al., 2023) and an extensive repertoire of lineage-specific neuropeptides not found in other metazoans (Hayakawa et al., 2022; Sachkova et al., 2021). Notably, early genomic and single-cell transcriptomic studies failed to identify conserved neuronal markers in ctenophores (Moroz et al., 2014; Sebé-Pedrós et al., 2018). It was only through the use of pro-neuropeptide-based markers that distinct neural cell types were molecularly identified (Hayakawa et al., 2022; Sachkova et al., 2021). In parallel, phylogenomic and chromosomal synteny analyses have suggested that ctenophores may represent the sister group to all other animals (Li et al., 2021; Ryan et al., 2013; Schultz et al., 2023; Whelan et al., 2015), raising the possibility that their nervous system evolved independently from those of other metazoans (Moroz, 2015). This hypothesis positions ctenophores as a key lineage for re-evaluating the origins and diversity of neural systems (Burkhardt and Jékely, 2021). However, without a detailed understanding of how ctenophore neurons are spatially organized and interconnected, it remains unclear how their nervous

system controls behaviour. Clarifying this relationship between neural architecture and behavioural control is essential to uncovering ctenophore neural function.

To address the lack of structural, circuit-level understanding of the ctenophore nervous system, we focused on a unique sensory structure—the aboral organ. This gravity-sensing organ contains a statocyst formed by lithocytes and four clusters of mechanosensory balancer cells, which act as pacemakers for the beating of comb-plate cilia and thereby control body orientation (Horridge, 1965; Tamm, 1980). A key feature of balancer cilia is their bidirectional, mechanoresponsive control of beat frequency. Depending on the direction of deflection and the animal's geotactic state, balancer cilia may either increase or decrease their activity, indicating a dynamic response system (Horridge, 1965; Tamm, 1982; Tamm, 2014a).

In the natural environment, most ctenophores can freely adjust their posture within the water column and exhibit both positively and negatively gravitactic orientations. This behavioral flexibility is likely supported by the aboral organ, which functions as a gravity sensor and pacemaker for ciliary movement. In this study, we focused on the orientation in which the aboral organ faces upward (“balancer-up” posture), as this configuration facilitates intuitive interpretation of balance-like functions and matches the setup used in high-speed imaging experiments.

Previous studies have implicated membrane potential, intracellular calcium concentration, and synaptic input in modulating the balancer response (Lowe, 1997). In particular, deflection-induced excitation can be abolished by calcium channel inhibitors or calcium-free conditions (Lowe, 1997), while high extracellular K⁺ depolarizes and activates cilia in the absence of mechanical stimuli (Lowe, 1997). Local calcium application further suggests that Ca²⁺ influx at the ciliary base may be required for the excitatory response (Lowe, 1997). These findings support the hypothesis that ionic currents and potential neural inputs play critical roles in shaping balancer-cell output (Lowe, 1997).

Ultrastructural and immunohistochemical studies have revealed that the aboral organ contains diverse sensory and neural components, including a distinct neural structure termed the deep nerve net (Aronova, 1974; Hernandez-Nicaise, 1968; Jager et al., 2010). However, how this deep nerve net regulates balancer or other functions has remained elusive.

To investigate how balancer cilia are modulated within the aboral organ, we combined volume electron microscopy (vEM) and high-speed imaging in the ctenophore *Mnemiopsis leidyi*. Through connectomic reconstruction, we characterized the synaptic architecture of the aboral nerve net, revealing synaptic inputs to the balancer cells. By functional imaging, we uncovered correlated activity patterns in balancer cilia across the four quadrants of the apical organ. Our results suggest that the aboral nerve net functions in coordinating the activity of balancer cilia, rather than fulfilling a feedforward sensory-motor function.

Results

Volume EM reconstruction of the *Mnemiopsis* aboral organ

For vEM analysis, we used a five-day-old cydippid larva of *Mnemiopsis leidyi*. To ensure optimal ultrastructural preservation, the specimen was prepared by high-pressure freezing, followed by freeze substitution and Epon embedding. From the aboral tip, we collected ~1,000 ultra-thin (50 nm) serial sections as ribbons, targeting only the region containing the aboral organ. These were imaged using a Zeiss Gemini 500 SEM at a pixel size (xy) of 2.0 nm. We imaged only the region containing the aboral organ. Subsequently, images from 620 layers were stitched and aligned in TrakEM2 (Cardona et al., 2012). The final vEM dataset encompassed a volume of 60 μm × 40 μm × 30 μm. We skeletonised and annotated all cells in this dataset in CATMAID (Saalfeld et al., 2009; Schneider-Mizell et al., 2016). We reconstructed 972 cells with intact nuclei and somata. Among these, 898 were located within the aboral organ (AO), including balancers and the aboral nerve net neurons (Video 1). Due to the compact and mostly self-contained organization of the AO, these cells were largely contained within the imaged

volume. We classified these cells into cell types (Figure 1–figure supplement 1, Figure 1–figure supplement 2).

In cells containing cilia, we also traced cilia along their length and annotated all basal bodies (Video 2 and not shown). For neuronal skeletonization, nodes were placed to interconnect the profiles of the same neuron's processes across layers, extending the skeleton until all branches were fully traced. All nodes relevant to synaptic sites were tagged, and skeletons were named and assigned multi-level annotations. As described later, some neurons formed loop-like structures (anastomosed neurons), in which separated branches often rejoined either the main branch or smaller branches (Burkhardt et al., 2023). Since CATMAID only supports skeleton trees, branch nodes in such cases were placed near the closest existing node and annotated accordingly. The entire skeletonized volume was composed of 134,591 nodes. 73 fragments could not be attached to somata-associated skeletons. Most of these fragments represent short skeletal branches that could not be traced beyond gaps or low-quality layers.

Next, we divided the entire aboral organ into four quadrants (Q1–Q4) to facilitate grouping the identified cells (Figure 1G) (Martindale and Henry, 1999). The general body plan of ctenophores, when viewed from the aboral side, exhibits biradial symmetry around the anal pores (Martindale and Henry, 1999). This symmetry corresponds to the four blastomeres present at the four-cell stage during early embryonic development (Martindale and Henry, 1999). We assigned each of the 898 skeletonised AO cells to one of the four quadrants (Figure 1G).

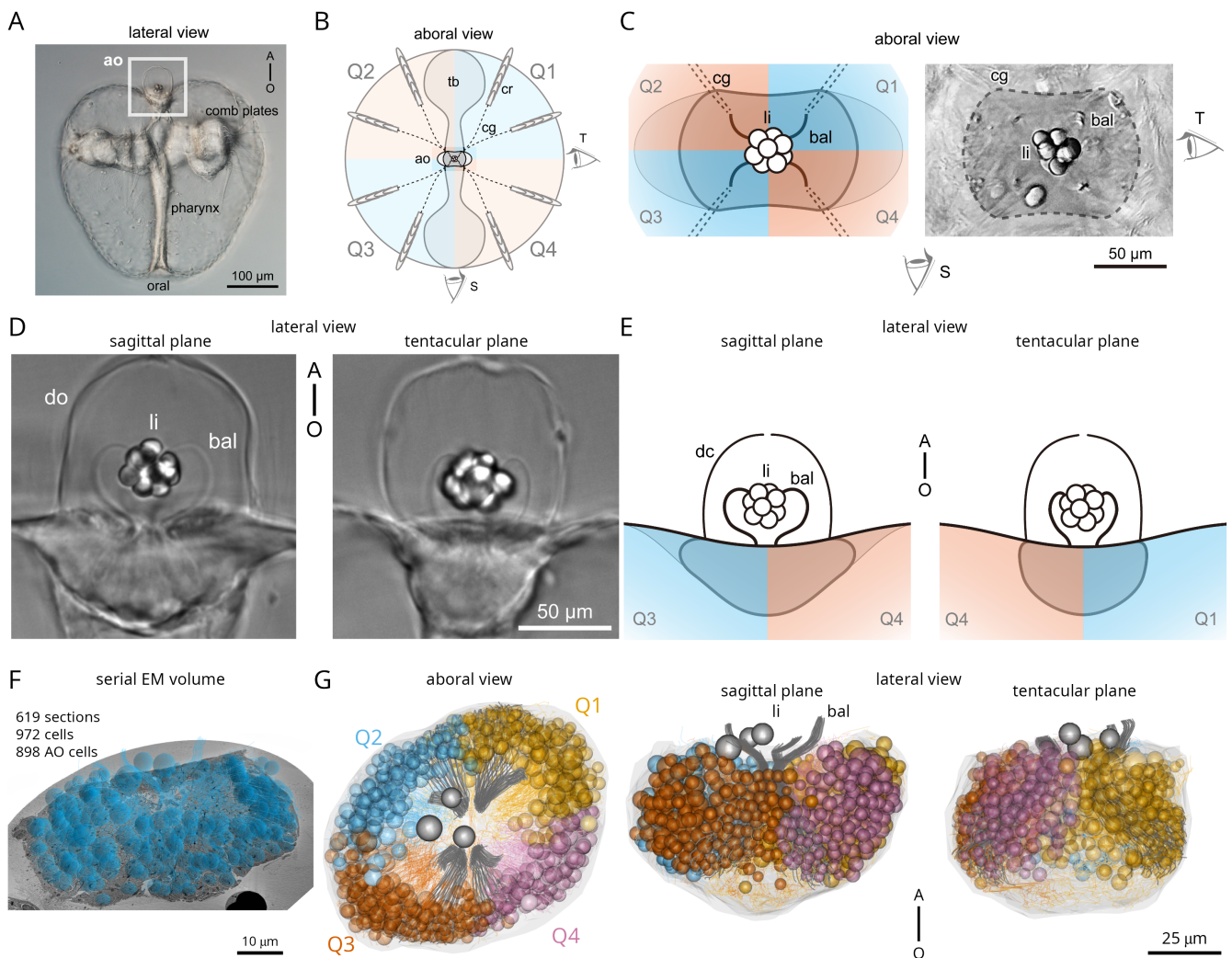


Figure 1. Morphology of the aboral organ in *Mnemiopsis leidyi*

(A) Whole-body image of a 5-day-old *M. leidyi* cydippid larva in lateral view. The boxed region indicates the aboral organ (ao). Scale bar: 100 µm.

(B) Schematic diagram of the aboral view of a cydippid larva. The two-tone coloration represents the biradial symmetry of the body. For convenience, the body is divided into four quadrants, designated as the first (Q1) through fourth (Q4) quadrants. The two primary viewing angles are referred to as the sagittal plane (S) and the tentacular plane (T). Abbreviations: ao, aboral organ; cg, ciliated groove; cr, comb plates; tb, tentacle bulbs.

(C) Aboral views of the aboral organ highlighting its spatial organization. The left panel presents a schematic representation of the aboral organ, illustrating the four body quadrants (Q1–Q4), color-coded consistently with panel (B). The right panel shows a corresponding differential interference contrast (DIC) image from the same perspective. The region enclosed by the dotted line delineates the boundary of the aboral organ. The sagittal (S) and tentacular (T) arrows indicate the viewing directions corresponding to those planes. Scale bar: 50 µm. bal, balancer; cg, ciliated grooves; li, lithocyte.

(D) Lateral views of the aboral organ in two orthogonal planes captured using DIC microscopy. The left panel shows a lateral view in the sagittal (S) plane, while the right panel displays a view in the tentacular (T) plane. Balancer cilia (bal) and lithocytes (li) are enclosed within the dome (do). Scale bar: 50 µm. A–O indicates the aboral–oral body axis.

(E) Schematic representations of the aboral organ in sagittal and tentacular planes. The left panel shows a lateral schematic in the sagittal plane (S), and the right panel shows the same in the tentacular plane (T), corresponding to the views in panel (D). Colors match the quadrant scheme shown in panels (B) and (C).

(F) Example of cell tracing in CATMAID. The spherical objects indicate nuclear positions, while the lines represent the traced cell centers. Scale bar: 10 µm.

(G) Morphological rendering of cells composing the aboral organ displayed in aboral view (left panel), sagittal plane view (middle panel) and tentacular plane view (right panel). Cells are color-coded according to quadrants. Lithocytes (li) are represented as three gray spheres, balancers (bal) are depicted as gray lines. Scale bar: 25 µm.

An aboral synaptic nerve net of syncytial neurons

Previous immunofluorescent staining in *Pleurobrachia pileus* suggested the presence of a nerve net at the base of the aboral organ, possibly continuous with the surrounding epithelial nerve net (Jager et al., 2010). Electron microscopy studies later revealed synapses near the floor of the aboral organ, a region where densely packed epithelial cells form a floor-like structure (Hernandez-Nicaise, 1973; Horridge and Mackay, 1964).

In our volume EM dataset, we identified 428 synapses based on the canonical presynaptic triad morphology: a cluster of synaptic vesicles, a smooth endoplasmic reticulum cisterna, and a mitochondrion. At synaptic sites, we marked mitochondria as synaptic nodes (orange in CATMAID) and connected this node to the nearest node in postsynaptic cells across the regions where synaptic vesicles aligned with the presynaptic cell's membrane, as indicated by light blue arrows in CATMAID (Figure 2–figure supplement 1A). No specialized postsynaptic densities were observed, consistent with prior reports (Hernandez-Nicaise, 1973). Synapses were either monoadic (one postsynaptic target) or polyadic (multiple postsynaptic targets) (Figure 2–figure supplement 1B).

We reconstructed three aboral nerve-net (ANN) neurons, each exhibiting a syncytial morphology characterized by anastomosing membranes and multiple nuclei (ranging from two to five) (Figure 2A and B, Figure 2–figure supplement 1C). These ANN neurons are morphologically distinct from the previously described syncytial subepithelial nerve net (SNN) neurons in the body wall of *Mnemiopsis*, which show a blebbed morphology and contain abundant dense core vesicles (Burkhardt et al., 2023). Our results identify a second type of syncytial neuron in *Mnemiopsis*. In addition to the previously characterized SNN neurons in the body wall, we observed ANN neurons within the aboral organ. Unlike SNNs, which exhibit a blebbed morphology and contain numerous dense core vesicles, ANN neurons are smooth-surfaced and lack dense vesicles. ANN neurons were located centrally within the aboral organ, while SNN neurons were reconstructed near its periphery (Figure 2–figure supplement 1C–G).

Furthermore, ANNs are also different from other neurons previously reported by EM, including mesogleal neurons and ciliated sensory cells that synapse on the SNN (types 1–4) (Burkhardt et al., 2023). Based on soma size and spatial distribution, we classified ANN neurons into two types. The first is a single large neuron, ANN_Q1–4, spanning all four quadrants and containing four (possibly five) nuclei. This neuron formed 150 presynaptic sites. The second type includes two smaller neurons, ANN_Q1Q2 and ANN_Q3Q4, each confined to two adjacent quadrants and containing two nuclei. ANN_Q1Q2 had 119 presynapses, while ANN_Q3Q4 had 68 (Figure 2C–F). In contrast, SNN neurons exhibited either no synaptic contacts or only a few.

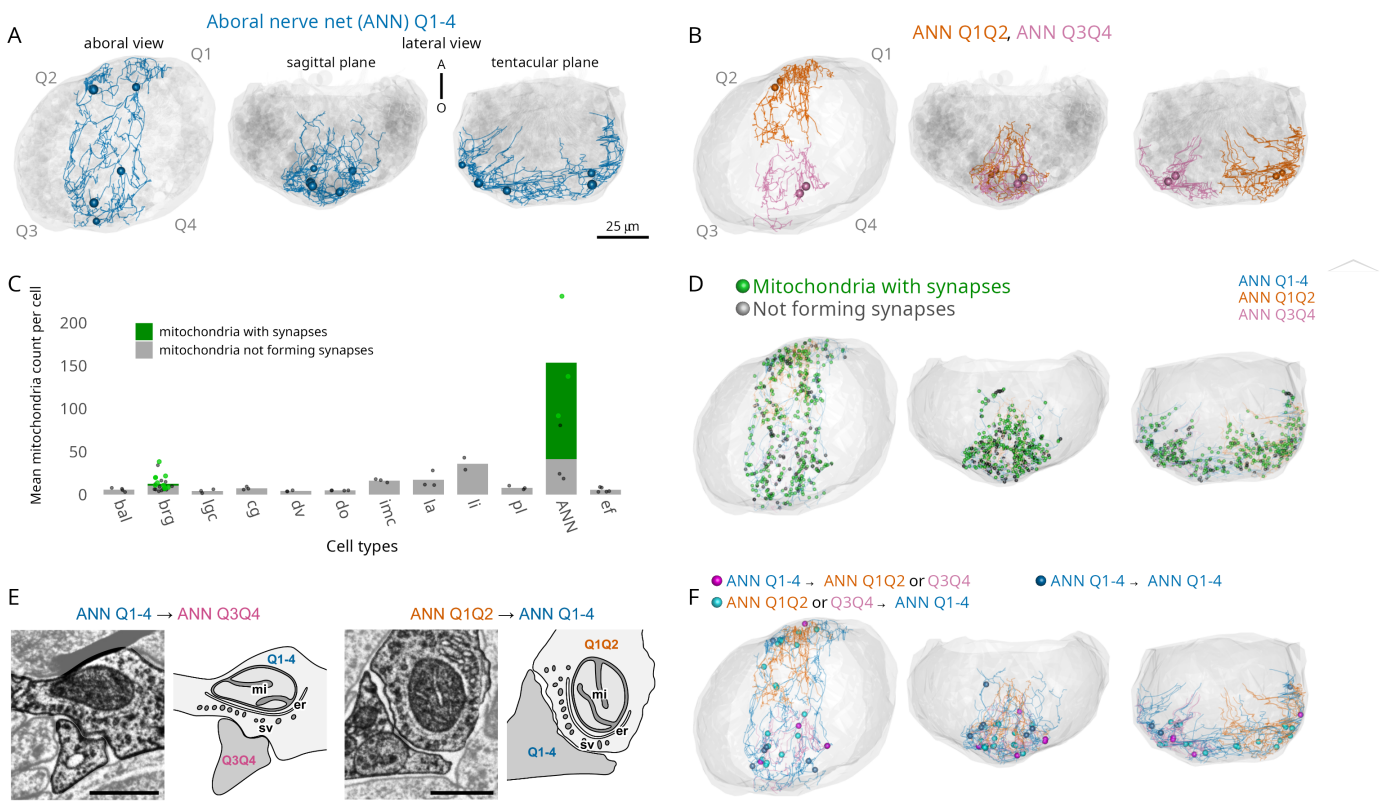


Figure 2. Organisation of the aboral synaptic nerve net

(A) Morphological rendering of the large aboral nerve-net neuron ANN_Q1-4 spanning all four quadrants, in aboral view (left), sagittal view (middle panel) and tentacular view (right panel). Spheres indicate the positions of nuclei.

(B) Morphological rendering of the two smaller ANN neurons ANN_Q1Q2 (pink) and ANN_Q3Q4 (orange), each spanning two quadrants, in aboral view (left), sagittal view (middle panel) and tentacular view (right panel). Spheres indicate the positions of nuclei.

(C) Number of mitochondria per cell for each cell type. The number of synapse-associated mitochondria is shown in green, the number of mitochondria outside synapses is shown in grey. N > 2 cells for each cell type except lithocytes. Abbreviations: bal, balancer; brg, bridge; lgc, large granular cell; cg, ciliated groove; dv, dense vesicle cells; imc, intra-multiciliated cells; la, lamellate bodies; li, lithocytes; pl, plumose; ef, epithelial floor cells.

(D) Position of mitochondria within ANN_Q1-4. Red indicates mitochondria associated with the presynaptic triad structures, yellow marks mitochondria containing synaptic vesicles but lacking a clearly defined presynaptic triad, blue represents mitochondria with unclear synaptic vesicles, and black denotes mitochondria where no synaptic vesicles were identified.

(E) Representative electron micrographs of presynaptic triad structures observed in the dataset and their schematic diagrams. The left diagram illustrates synaptic projections from the center ANN (ANN Q1-4) to the lateral ANN (ANN Q3Q4), while the right diagram shows synaptic projections from the lateral ANN (ANN Q1Q2) to the center ANN (ANN Q1-4). Abbreviations: mi, mitochondrion; er, endoplasmic reticulum; sv, synaptic vesicles. Scale bar: 500 nm.

(F) Position of synapses. Synapses from the center ANN to the lateral ANN are shown in magenta, while synapses from the lateral ANN to the center ANN are shown in cyan. Blue dots indicate the locations of autapses within ANN_Q1-4.

Synaptic connectome of the gravisensory organ

Synapse annotation revealed multiple types of connections involving ANN neurons within the gravisensory organ, including reciprocal ANN–bridge cell connections, ANN autapses, and outputs to balancer cells. We identified synapses between different ANN neurons and synapses that ANN_Q1-4 forms on itself (autapses). The ANN neurons also form synapses on the gravity-sensing balancer cells and the bridge cells, but not balancer cells, also synapse on the ANN.

Balancer cells are monociliated cells with long motile cilia that form four bundles of compound cilia, one in each quadrant (Video 2). These bundles come together at the centre of the aboral organ to support the cellular mass of the statolyth. The bending of the cilia and the position of somata differed clearly when viewed laterally from the sagittal or the tentacular plane (Figure 3B). In each quadrant, there were

between 28–37 balancer cells (Q1: 37; Q2: 32; Q3: 32; Q4: 28). Each cell contained 3 to 10 mitochondria.

ANN_Q1-4 formed synapses on balancer cells in all four quadrants (on 7 cells in Q1, 11 cells in Q2, 6 cells in Q3 and 10 cells in Q4) while ANN_Q1Q2 and ANN_Q3Q4 synapsed to balancer cells in their respective quadrants (ANN_Q1Q2 on 6/37 cells in Q1 and 8/32 cells in Q2; ANN_Q3Q4 on 1/32 cells in Q3 and 5/28 cells in Q4). Some balancer cells received inputs from both ANN_Q1-4 and either of ANN_Q1Q2 or ANN_Q3Q4. Notably, we found no presynaptic sites in balancer cells (Figure 3 – figure supplement 1), contradicting earlier suggestions of afferent signaling from balancer cells to neurons ([Hernandez-Nicaise, 1974](#)).

The second group of cells that formed synaptic contacts with the ANN were the bridge cells. Bridge cells, first described in 2002 ([Tamm and Tamm, 2002](#)), are characterized by bundles of elongated processes filled with microtubules that arch over the epithelial layer, resembling a bridge. Their somata are located at the base of the paired balancer-cell clusters along the tentacle surface and extend across the sagittal plane towards the base of the opposite balancer cells. Bridge cells form two distinct cell groups across the sagittal plane, in the Q1Q2 and Q3Q4 regions. In the Q1Q2 region, we identified 14 bridge cells, in Q3Q4, 12 cells (Figure 3 – figure supplement 1, Video 1).

In contrast to balancer cells, bridge cells participated in reciprocal synaptic interactions with ANN neurons, forming both pre- and postsynaptic connections.

Nearly all bridge cells (25/26) received synaptic input from ANNs. Bridge cells in Q1Q2 received inputs from ANN_Q1Q2 (11 cells), ANN_Q1-4 (1 cell), or both (2 cells). In Q3Q4, synapses on bridge cells were from ANN_Q3Q4 (1 cell), ANN_Q1-4 (7 cells), or both (1 cell).

Bridge cells also had presynaptic sites with the typical presynaptic triad structure near 30% of their mitochondria. These bridge-cell synapses were formed on ANN neurons or other bridge cells. Bridge cells in the Q1Q2 region formed synapses on ANN_Q1Q2 (3 cells) or on both ANN_Q1Q2 and ANN_Q1-4 (2 cells). Bridge cells in Q3Q4 synapsed on ANN_Q3Q4 (1 cell) or ANN_Q1-4 (6 cells).

In both the Q1Q2 and the Q3Q4 regions, bridge cells also formed synapses with adjacent bridge cells. However, we found no synapses across the sagittal plane to bridge cells in the opposite region.

To examine the overall synaptic organization of the balancer organ, we grouped cells of the same type and region into network nodes, summed the synaptic counts, and mapped the network onto the four-quadrant anatomy (Figure 3H). The resulting connectivity graph revealed feedback loops among ANN neurons and between ANN and bridge cells, displaying rotational symmetry. Local sub-circuits centered around ANN_Q1Q2 and ANN_Q3Q4 were evident, while ANN_Q1-4 formed global connections across quadrants.

Surprisingly, and contrary to the expected sensory–motor or input–output model of balancer function, we found no synapses from the mechanosensory balancer cells to ANN neurons, nor from ANN neurons to known motor effectors such as ciliated groove cells.

The ANN neurons also formed synapses on other cell types in the aboral organ, including the dense-vesicle cells, epithelial floor cells and several non-ciliated, monociliated or biciliated cells (Figure 3 – figure supplement 1). None of these other cell types synapsed on the ANN. These cell types and synaptic connections are outside the gravisensory organ and are not considered further here.

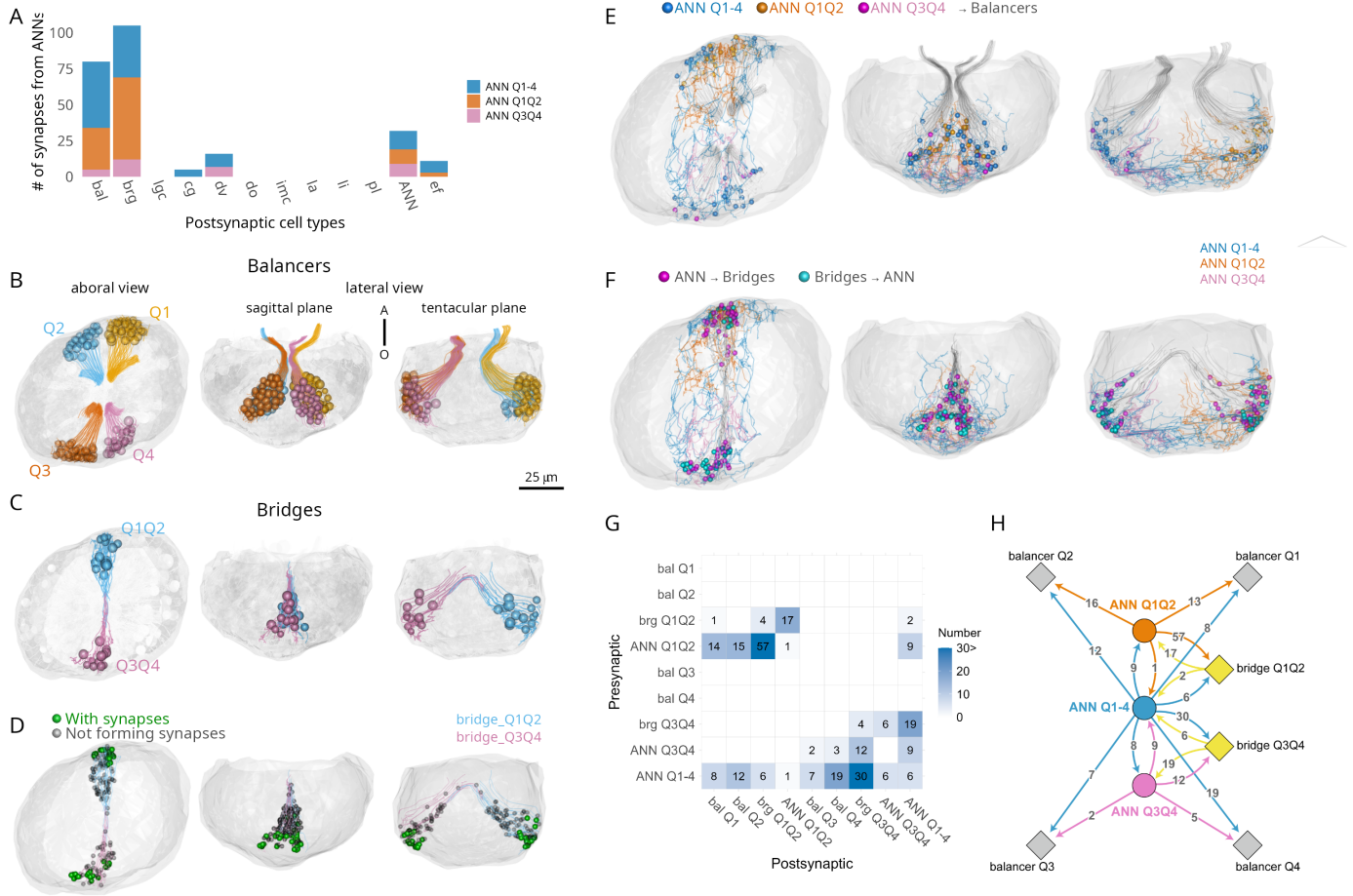


Figure 3. Synaptic connectivity of the balancer and bridge cells with the ANN.

(A) Number of synaptic inputs from the ANNs (ANN_Q1-4: blue, ANN_Q1Q2: orange, ANN_Q3Q4: pink) to each cell type. Abbreviations: bal, balancer; brg, bridge; lgc, large granular cell; cg, ciliated groove; dv, dense vesicle cell; imc, intra-multiciliated cell; la, lamellate body; li, lithocyte; pl, plumose cell; ef, epithelial floor cell.

(B) Morphological rendering of balancer cells, with each cell color-coded by quadrant: Q1 (yellow), Q2 (blue), Q3 (orange), and Q4 (magenta). Each sphere represents the position of an individual nucleus. The fine projections extending from the cells represent traced trajectories that follow the cell body and continue into a single cilium from the point where it emerges. Views are shown from three orthogonal perspectives: aboral view (left), sagittal plane (middle), and tentacular plane (right). The spatial arrangement highlights the quadrant-specific organization of balancer clusters within the aboral organ. Scale bar: 25 μm.

(C) Morphological rendering of bridge cells spanning the Q1Q2 and Q3Q4 quadrants. The Q1Q2-side bridge cells (8 cells) are shown in blue, while the Q3Q4-side bridge cells (6 cells) are shown in xxx color. The morphology of individual bridge cells extending across opposite quadrant regions is depicted. The spheres represent the positions of individual nuclei. The left panel shows an aboral view of the aboral organ, the middle panel presents a sagittal plane view, and the right panel provides a tentacular plane view.

(D) Mitochondrial localization within bridge cells and associated presynaptic triad structures. Red indicates mitochondria associated with presynaptic triad structures, yellow marks mitochondria containing synaptic vesicles but lacking a clearly defined presynaptic triad, blue represents mitochondria with unclear synaptic vesicles, and black denotes mitochondria where no synaptic vesicles were identified. The left panel shows a dorsal view of the aboral organ, the middle panel presents a sagittal plane view, and the right panel provides a tentacular plane view.

(E) Synaptic connections from ANNs to balancer ciliated cells. The positions of synapses from ANNs to balancers (magenta) are indicated. The left panel presents an aboral view, while the right panel shows a lateral view and a tentacular plane view. Balancer ciliated cells are depicted in light gray.

(F) Synaptic connections between ANNs and bridge cells. The positions of synapses from ANNs to bridge cells (magenta) and from bridge cells to ANNs (light blue) are indicated. The left panel shows an aboral view, while the right panel presents a tentacular plane lateral view. Bridge cells are shown in light gray.

(G) Connectivity matrix of the gravity-sensing neural circuit. Columns represent presynaptic cell groups, while rows represent postsynaptic cell groups. The numbers and varying shades of blue correspond to the number of synapses.

(H) Complete connectivity map of the gravity-sensing neural circuit. Cells belonging to the same group are enclosed in hexagons, and the number of cells is added to their labels. The thickness of the arrows and the numerical values indicate the number of synapses. ANNs in Q1Q2 are shown in blue, ANNs in Q3Q4 in pink, balancer cell groups in gray, and bridge cell groups in yellow.

Dynamics of balancer cilia imply a coordinating function for the nerve net

To investigate whether balancer cilia are coordinated by neural inputs, we did high-speed video microscopy recordings to analyze their activity patterns across body axes. Previous studies ([Lowe, 1997](#); [Tamm, 1982, 1980](#)) have established that balancer cilia function as mechanoreceptors, with their beating frequency modulated by inclination.

Tamm also suggested that differences in statolith morphology and the shape of balancer cilia between the tentacular and sagittal planes could lead to different forces exerted on cilia by the statolith ([Tamm, 2015, 2014b](#)). To further explore this, we used a tilted microscope with a vertical stage where we mounted immobilised cydippid larvae with their aboral-oral axis aligned in different orientations relative to the gravity vector (Videos 3-7). We could confirm earlier finding that the beating frequency of balancer cilia is dependent on the inclination (Video 7). Our aim here was to focus on spontaneous ciliary beating under conditions of equal load from the statolith across quadrants. Therefore, we only analysed larvae whose aboral-oral axis was approximately parallel to the gravity vector (mouth facing downward within a 0–20° deviation). We then compared larvae oriented either with their sagittal or tentacular plane parallel to the sample stage (Figure 4A).

In larvae with their sagittal plane facing the objective, we could compare balancer-cilia movements between Q1(4) and Q2(3). In other larvae oriented in the tentacular plane, we could simultaneously image Q1(3) and Q2(4). We used a high-speed camera and recorded at 100 fps for 2 minutes (12,000 frames). To analyse ciliary beating, we selected regions of interest (ROIs) in areas where brightness changes indicated ciliary beating. Ciliary beating was both manually quantified and plotted as kymographs.

During the two-minute recordings, balancer cilia could beat fast, slow, or exhibit abrupt stops of beating (“arrest”) followed by re-initiation (“re-beat”). Occasionally, large body-contractions moved the entire cydippid out of frame, and data from these episods were excluded. We focused on three metrics for inter-quadrant comparison: (1) the timing of ciliary arrest, (2) the timing of re-beat after an arrested phase, and (3) ciliary beat frequency.

We found that arrest and re-beat events were synchronized between balancers across the sagittal plane. However, while the timing of re-beat was also near-simultaneous along the tentacular plane, arrest timing was offset by up to 2.16 seconds (Figure 4D, Videos 3-6). Overall, these data reveal that arrests are only coordinated between Q1-Q2 and Q3-Q4, whereas re-beat is coordinated over all four quadrants.

As shown in Figure 4E (and Figure 4–figure supplement 1), beat frequencies of left and right balancers fluctuated substantially in both orientations. However, while left-right activity was largely synchronized in sagittal pairs (Figure 4E, left), tentacular pairs (Figure 4E, right) displayed strikingly periodic alternations between left and right balancer activity. This pattern suggests a consistent temporal offset between the two sides, possibly arising from differences in the timing of arrest or re-beat events.

To quantify this, we calculated a rolling Pearson correlation between left and right balancer activity in each plane. The resulting mean correlations were significantly higher in the tentacular plane compared to the sagittal plane (Figure 4F; t-test, $p = 0.014$). This result indicates that tentacular balancers beat in a more coordinated, mirror-symmetric manner, whereas sagittal balancers exhibit greater variability between sides.

Evaluating these data in light of the circuit diagram suggests that shared ANN inputs (ANN_Q1Q2 or ANN_Q3Q4) to a pair of balancers along the sagittal plane may underlie their synchronized arrests. In contrast, in the tentacular plane, separate ANNs innervate the balancer pairs. At the same time, the ANN_Q1-4 neuron synapses on all four balancers, hinting at a neural substrate for their synchronised re-beat.

Notably, bridge neurons associated with each quadrant region (Q1Q2 or Q3Q4) extend their processes across the midline, forming connections that span between opposite quadrant domains when viewed along the tentacular plane. This morphology suggests a potential role for bridge neurons in modulating

inter-quadrant coordination. By linking ANN activity across orthogonal planes, these neurons may contribute to the dynamic regulation of CBF patterns by facilitating the spread of activity across orthogonal planes, thus supporting coordinated beating throughout the aboral organ.

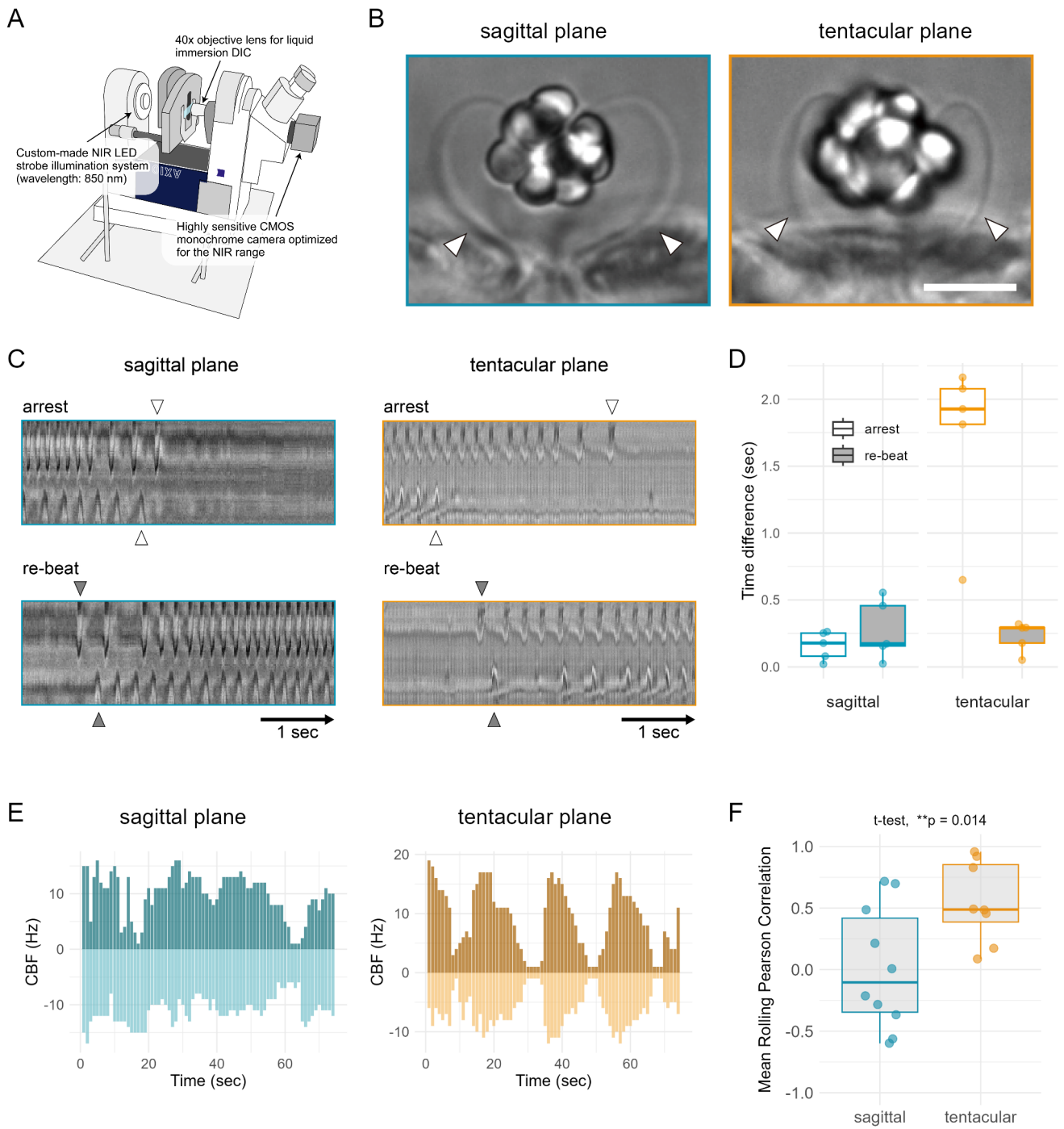


Figure 4. Analysis of ciliary beating, arrests and re-beat across balancers in the four quadrants

(A) Schematic diagram of the differential interference contrast (DIC) microscopy setup used to image the movement of balancer cilia. The microscope was tilted 90 degrees so that the stage was positioned vertically. We used a 40x objective lens and a monochrome CMOS camera sensitive to near-infrared (NIR) light that was synchronized with an 850 nm strobe light source.

(B) Representative DIC images of the aboral organ viewed along the sagittal (left) and tentacular (right) planes. Arrowheads indicate the balancer cilia selected for kymograph-based analysis in each orientation. Scale bar: 25 μm .

(C) Representative kymographs showing arrest and re-beat events of balancer cilia. Left and right balancer cilia were simultaneously recorded in either the sagittal (left) or tentacular plane (right). Arrowheads mark the onset of arrest (open) and re-beat (filled); horizontal arrows represent 1-second intervals.

(D) Boxplots showing time differences in the onset of arrest (white boxes) and re-beat (grey boxes) between left and right balancer cilia. Colors of the box outlines indicate the imaging plane: sagittal (blue) or tentacular (orange). Each dot represents a single larva.

- (E) Bar plots showing ciliary beat frequency (CBF) dynamics of left and right balancers (top and bottom, respectively) recorded from the sagittal (left) or the tentacular (right) planes. Positive and negative values represent opposite sides within each plane.
- (F) Mean rolling Pearson correlation of left–right balancer CBF calculated with a 20-frame window. Each dot represents an individual larva. Balancers on the tentacular plane showed significantly higher correlation than those on the sagittal plane (t-test, $p = 0.014$).

Discussion

An Aboral Nerve Net for Ciliary Coordination

In this study, we generated the first high-resolution connectome of the ctenophore nervous system by reconstructing approximately 900 cells from the aboral organ of a five-day-old *Mnemiopsis leidyi* cydippid by volumetric electron microscopy. Among the reconstructed cells, we identified a previously undescribed type of syncytial neuron—here referred to as aboral nerve net (ANNs)—with multiple nuclei. The ANN has a morphology distinct from that of the subepithelial nerve net (SNN) reported for one-day-old cydippids (Burkhardt et al., 2023; Sachkova et al., 2021). A parallel vEM study of a one-day-old cydippid also identified a distinct subtype of SNN neurons in the aboral region, termed “condensed” SNN, which display a more compact morphology compared to body wall SNNs (Ferraioli et al., 2025). However, the ANN neurons described here are morphologically and anatomically distinct from both the body wall SNN and the condensed SNN in the earlier stage. Instead of forming discrete nodal swellings or a “beads-on-a-string” organization typical for the SNN, ANNs extend through intercellular spaces, weaving between neighboring cells in a smooth, interdigitating fashion. The presence of two SNN-type neurons more laterally in the aboral organ in our dataset (Figure 2–figure supplement1) further underline the distinct identity of ANNs.

ANNs form no synaptic output to classical effector organs such as muscles or comb plates. All observed output synapses were directed to balancer ciliary cells, bridge cells or other sensory cells. This suggests that ANNs are unlikely to serve as motor drivers (premotor neurons or motoneurons) in the conventional sense. Rather, they may be involved in coordinating or modulating the timing and dynamics of the activity of the sensory-motile balancer cilia, possibly modulating their responsiveness to statocyst load (Keijzer et al., 2013; Verasztó et al., 2017; Wiljes et al., 2015).

What could be the function of the aboral nerve net? We found differences in the innervation patterns of ANNs across the sagittal and tentacular planes. The two smaller ANNs targeted a pair of balancers (either Q1-Q2 or Q3-Q4) across the sagittal plane. This innervation pattern corresponded with plane-specific differences in the dynamics of balancer cilia. Across the sagittal but not the tentacular plane, the closures of balancer cilia were near-simultaneous, within less than one beat phase. In contrast, the large ANN innervated balancers in all four quadrants and could account for the near-simultaneous re-beat (within less than one beat phase) of the four balancers. The neurotransmitter identity and activation dynamics of these neurons remains unresolved. However, the combination of circuit architecture and behavioural outputs provides the first functional insight into the role of neurons in a ctenophore.

The functional organisation of the ANN circuit is reminiscent of the ciliomotor circuit in the larvae of the marine annelid *Platynereis dumerilii*. Here, the activation of cholinergic motor neurons leads to the synchronous arrest of cilia on multiple multiciliary bands (Verasztó et al., 2017). This is antagonised by serotonergic midline-crossing neurons that drive ciliary re-beat (Calderón et al., 2024; Verasztó et al., 2017). The ctenophore balancer-circuit is the second synaptically mapped ciliomotor circuit that convergently evolved analogous control mechanisms to the annelid and other ciliomotor systems (Marinković et al., 2019; Moroz, 2015; Roberts et al., 2022).

Overall, our findings suggest that the ANN network has a coordinating function to synchronize the activity of balancer cilia thereby possibly fine-tuning their activity or resetting their sensitivity. This departs fundamentally from reflex-arc models of simple nervous systems (Arendt, 2021; Jékely, 2010) and instead supports the idea that coordination, not command, may have been a foundational role of

ancestral neurons (Keijzer et al., 2013). Such an organisation may have been retained in modern ctenophores ever since they evolved a pelagic lifestyle and a balancer (Stanley and Stürmer, 1983).

A

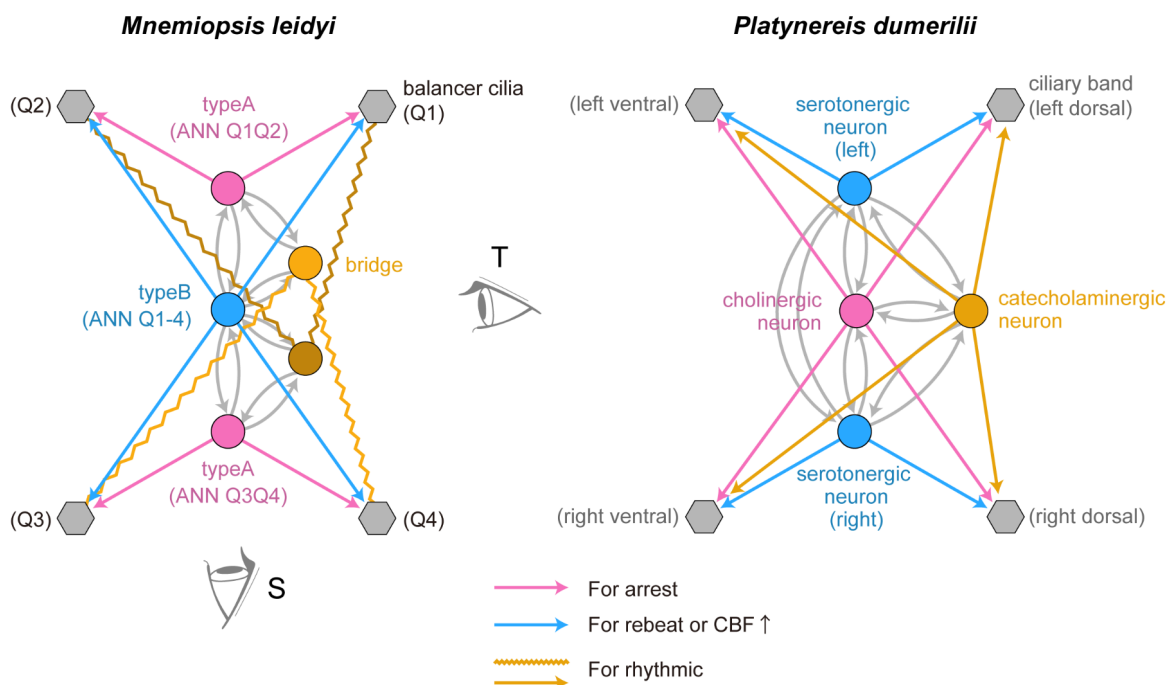


Figure 5. Comparison of Neural Circuits Regulating Ciliary Movement

(A) Neurons are represented by circles, color-coded to indicate analogous functions in ciliary control. Ciliated cells are shown in gray. Synapses are indicated by arrows, with magenta representing synapses that induce ciliary arrest and blue representing synapses that induce ciliary re-beat or an increase in ciliary beating frequency.

(Left) Neural circuit of the *M. leidyi* gravi-sensory organ. Bridge cells (yellow squares) are suggested to be electrically coupled (indicated by yellow zigzag lines), implying a potential involvement in feedback mechanisms between neurons and ciliated cells.

(Right) Neural circuit regulating prototroch ciliary movement in *P. dumerilii*. Serotonergic neurons (Ser-h1 neurons, blue) activate ciliary movement, while a cholinergic neuron (MC neuron, magenta) induces ciliary arrest.

Bridge Cells as Feedback Regulators of Ciliary Rhythms

In our volumetric reconstruction, bridge cells were identified as the only cell type providing synaptic input to the ANN network, positioning them as key upstream regulators of the ciliary coordination system in the aboral organ. Originally described morphologically by Tamm et al. (2002), bridge cells extend thin projections towards the base of the balancer cilia (Tamm, 2014a; Tamm and Tamm, 2002). Based on this spatial relationship, they may receive information about the physical state of the cilia—such as mechanical load or phase—or possibly local field potential (LFP) changes (Jurisch-Yaksi et al., 2024; Sheu et al., 2022). These features suggest that bridge cells may act as transducers, converting local ciliary signals into neural inputs directed towards the ANN circuit.

As revealed by our high-speed imaging, ciliary beat frequency (CBF) exhibited rhythmic changes over time that differed between anatomical planes (Figures 4E and F), indicating spatially distinct coordination dynamics. These CBF rhythms are likely generated by the ANN circuit, while bridge cells may function to stabilize or adjust this rhythmic output in accordance with the real-time state of the cilia. This way, bridge cells may provide feedback about the state of their cilia to the coordination circuit, serving as a core element of a self-regulating rhythm-control system.

This architecture can be interpreted as a recurrent information loop, in which output from the ANN circuit modulates ciliary activity, and the resulting ciliary state is in turn relayed back to the ANN via bridge cells. Such a structure suggests a loop-based coordination mechanism (Arshavsky, 2003; Selverston, 2010), where the central circuit adapts its timing based on feedback from its target. Although the electrophysiological properties of bridge cells remain to be elucidated, their recursive integration into the ANN circuit indicates that they may function in maintaining the robustness and flexibility of endogenous ciliary rhythms (Kennedy and Weissbourd, 2024).

Conclusion

How do differences in balancer cilia coordination across anatomical planes shape behaviour? In *Mnemiopsis*, the animal swims upright with its mouth facing upward, and performs 90-degree rotational turns when hunting prey or responding to disturbances (Colin et al., 2010; Courtney et al., 2020; Waggett, 1999). Large rotational maneuvers may involve balancer cells in the tentacular plane, while sagittal-plane balancers may contribute to postural stabilization (Tamm, 2015).

Our findings reveal a circuit composed of ANN neurons and bridge cells that coordinates ciliary beating rhythms in space and time without direct sensory input, and features a recursive architecture in which ciliary outputs may feed back to the circuit via bridge cells. Such a configuration suggests that even with a limited number of cells, the system is capable of flexible and robust rhythm control.

As Jagar et al. (2011) once described, this organ evokes the metaphor of a “ciliary brain” (Jager et al., 2010). The network we describe here orchestrates output through dynamic, self-regulating coordination. Future work could uncover these dynamics, visualized through live imaging of the entire cell ensemble, to offer a window into the core functions of a unique nervous system.

Materials and Methods

Specimen Preparation, Volume Electron Microscopy, and Image Processing

Larvae of *Mnemiopsis leidyi* (five days old) were cryofixed using a high-pressure freezing apparatus (HPM Live μ , CryoCapCell, <https://www.cryocapcell.com/technologies/high-pressure-freezer>) and immediately transferred to liquid nitrogen for storage. The frozen samples were processed in a substitution medium containing 2% (w/v) osmium tetroxide and 0.5% uranyl acetate in acetone, using a cryo-substitution device (EM AFS-2, Leica).

Cryo-substitution was carried out by gradually raising the temperature from -90°C to -70°C over 4 hours, then returning to -20°C over 2 hours, and finally to room temperature over 2 hours. The samples were then embedded in epoxy resin (EMbed 812, Electron Microscopy Sciences).

Serial ultrathin sections of 50 nm thickness were prepared using a Leica UC7 ultramicrotome and a 45° DiATOME diamond knife. A conductive indium tin oxide-coated glass slide (ITO Glass, UQG Optics) was treated with air glow discharge using the PELCO easiGlow system (Ted Pella, Inc.) to enhance section adhesion and improve hydrophilicity. This process rendered the glass surface negatively charged.

Section ribbons were collected on prepared glass slides, gently dried to ensure proper stretching, and firmly adhered to the glass surface. The sections were stained with UranyLess and lead citrate (Reynolds) using airless staining procedures. The glass slides were mounted on a STEM-specific stage (Zeiss) using Copper Foil EMI Shielding Tape (3M).

Imaging was performed using a Gemini SEM 500 (Zeiss), equipped with SmartSEM and Atlas 5 imaging software (Zeiss), using the Inlens detector. A total of 620 serial sections, each 50 nm thick, were analyzed. The imaging resolution was 2.8 nm/pixel, and the acceleration voltage was set to 1.5 kV. The imaging time for each tile was 54 minutes and 21 seconds, with a pixel size of 2.8 nm, a tile size of 91.8 × 91.8 μm (32768 × 32768 pixels), and a dwell time of 3.0 μs .

Image-Stack Alignment and Export for CATMAID

To process the image stack, we utilized the TrakEM2 plugin of FIJI (ImageJ) (version 2.0.0-rc-15/1.49k / Java 1.6.0_24 (64-bit) – 2014). A project was created, and all TIFF images were imported using the “import sequence as grid” function. Subsequently, the following filters were applied sequentially: Invert, Equalize Histogram, and Gaussian Blur.

The alignment process consisted of three stages, each progressively refining the spatial accuracy (rigid, affine, elastic).

Initially, a rigid alignment was run with the following parameters: least squares mode (linear feature correspondences), encompassing the entire layer range with the first layer as the reference. Only visible images were used, without propagation. The alignment was executed with an initial Gaussian blur of 1.6 pixels, three steps per scale octave, a minimum image size of 512 pixels, and a maximum of 2048 pixels. Additional parameters included a feature descriptor size of 8, orientation bins of 8, and a closest ratio of 0.92. The alignment allowed clearing the cache, using 32 feature-extraction threads, a maximal alignment error of 100 pixels, a minimal inlier ratio of 0.20, and a minimum of 12 inliers. The expected and desired transformations were set to rigid, with testing multiple hypotheses (tolerance: 5.00 pixels) and considering up to 5 neighboring layers, giving up after 5 failures. Regularization was done with a maximal iteration of 1000, a maximal plateau width of 200, and a rigid lambda of 0.10.

Next we applied an affine alignment step with similar parameters, except the expected and desired transformations were set to affine. The minimal image size was reduced to 64 pixels, while the other parameters (Gaussian blur, feature descriptor size, inliers, and testing hypotheses) remained unchanged to ensure consistent processing.

Finally, we ran two iterations of elastic alignment to fine-tune the spatial data. Key parameters included a block-matching layer scale of 0.05, a search radius of 200 pixels, a block radius of 2000 pixels, and a resolution of 60. Correlation filters were employed with a minimal PMCC r of 0.10, a maximal curvature ratio of 1000, and a maximal second-best r/best r of 0.90. A local smoothness filter was applied with the approximate local transformation set to affine, a local region sigma of 1000 pixels, and an absolute maximal local displacement of 10 pixels (relative maximal displacement: 3.00). Pre-aligned layers were tested for up to 4 neighboring layers. The elastic alignment used a rigid approximation, maximal iterations of 3000, a plateau width of 200, spring mesh stiffness of 0.01, and a maximal stretch of 2000 pixels. A legacy optimizer was employed to enhance performance.

After each alignment stage, the project was saved as an XML file under a unique name to preserve iterative progress. Finally, the images were exported from FIJI using TrakEM2 in a format compatible with CATMAID.

Neuron Tracing, Synapse Annotation, and Review

For skeletonisation, annotation and tagging we used CATMAID installed on a local server ([Saalfeld et al., 2009](#); [Schneider-Mizell et al., 2016](#)). To mark the locations of cell bodies, we placed tags at the approximate center of each nucleus within the dataset. At each nuclear center, the radius of the single node was adjusted according to the size of the cell body in that specific layer. All skeletons were rooted at their respective cell bodies, and the root nodes were tagged as “soma.” Synapses were identified based on four key structural features: the cell membrane, synaptic vesicles, the endoplasmic reticulum, and mitochondria. Most synapses could be verified across consecutive sections, ensuring accurate annotation and connectivity mapping.

Cell-type Nomenclature, Annotations and Connectome Analysis

We assigned each cell a specific cell-type name based on its morphological or functional category (e.g., balancer, bridge, large granular, ciliated grooves, dense vesicle cell, dome, epithelial floor (ef), intracellular multiciliated cells (imc), lamellate bodies (lb), lithocyte, plumose cell, and ANN), resulting in a total of 12 primary cell types.

In addition, some cells lacked distinctive features and were instead categorized into one of four general ciliated types, based on the presence and number of cilia: biciliated (biC), monociliated (monoC), multiciliated (multiC), or non-ciliated (non-C).

To indicate spatial positioning, we appended the quadrant number to the cell-type name using an underscore. For instance, cells located in the first quadrant were labeled “_Q1,” while those situated between two quadrants were labeled with both (e.g., “Q1Q2”).

Cells of the same type and in the same region were further distinguished by serial numbering, ensuring each cell has a unique identifier.

We further distinguished cells of the same type within the same region by serial numbering. This way each cell in the volume has a unique name string. Each cell was also assigned multiple annotations, which can be utilized to query the database via CATMAID or the CATMAID API (e.g., using the R catmaid package ([Bates et al., 2020](#))). These annotations provide a structured and precise framework for identifying and analyzing specific cells, facilitating robust data integration and retrieval from the dataset.

Imaging the Activity of Balancer Cilia

For ciliary imaging, we used the cydippid stage of *M. leidyi* at five days post-fertilization. A coverslip with a thin layer of Vaseline applied to its two edges was gently placed over a glass slide. Filtered natural seawater and cydippids were placed beneath the coverslip. The orientation of the larvae was adjusted by carefully sliding the coverslip, and the larvae were gently immobilized by applying slight pressure.

To ensure consistency in gravitational input, we selected only larvae whose aboral–oral axis was oriented nearly perpendicular to the gravitational vector (within 20° tilt). This minimized the potential influence of larval tilt on left–right differences in balancer cilia activity, as all balancers received comparable stimulation from the statolith.

This orientation corresponds to a “balancer-up” orientation, in which the aboral organ faces upward. We selected this configuration not only to ensure consistent stimulation from the statolith across individuals, but also because it facilitates intuitive interpretation of balancer function—as if balancing a stone on top. Moreover, this orientation matches the orientation used in electron microscopy and was technically advantageous for high-speed imaging under vertical-stage alignment. Using a consistent orientation throughout minimized potential confusion when comparing ultrastructural and functional data.

Because the tilt angle strongly affects the beat frequency of balancer cilia via asymmetric mechanical loading by the statolith ([Tamm, 1980](#)), our quantitative analysis was restricted to recordings that met the above orientation criterion (tilt < 20°). In this orientation, gravitational input from the statolith is approximately symmetrical across the left and right balancers, allowing meaningful comparisons of their activity. To illustrate how excessive tilt induces asymmetric stimulation, Video 7 presents two examples of larvae outside the permitted range: one tilted by ~135° in the sagittal plane and the other by ~60° in the tentacular plane. In both cases, strong asymmetries in balancer ciliary beating are evident, consistent with previous observations of gravity-induced geotactic responses ([Tamm, 1980](#)).

Balancer cilia movement was imaged using a differential interference contrast (DIC) microscope (Zeiss Axio Imager.M2) equipped with a 40x glycerine-immersion objective (LD LCI Plan-Apochromat 40x/1.2 Imm Corr DIC M27). Images were acquired with a high-sensitivity monochrome CMOS camera (UI-3360CP-NIR-GL Rev.2, iDS), optimized for near-infrared detection. Illumination was provided by a custom-built 850 nm LED strobe system, synchronized with camera exposure using BohNavi software. Recordings were acquired at 640 × 480 pixels, 100 frames per second (fps), for a duration of 2 minutes, using 0.05 ms pulse illumination from the LED.

For beat frequency analysis, kymographs were generated using the Multi Kymograph plugin in Fiji. One-second segments were manually extracted from the kymographs, and ciliary beat frequencies were visually counted for each manually defined region of interest (ROI). These manually determined frequencies were then used for subsequent computational analysis.

Traces of left and right cilia were extracted, cleaned to remove missing or non-finite values, and indexed by frame. Data were saved as RDS objects for downstream analysis. Mean values were plotted as bar graphs with left and right cilia plotted as positive and negative bars, respectively, to visually distinguish their activity.

To assess coordination between left and right cilia, we computed rolling Pearson correlation coefficients over a window of 20 frames. For each dataset, we excluded windows with insufficient valid data or no

variation. Time series of correlation coefficients were plotted and summarized as mean values. These mean correlations were then compared across planes (sagittal vs. tentacular) using Welch's t-test. The resulting statistics were visualized as boxplots with jittered data points.

Data and Code Availability

The EM image stacks, including all traces and annotations, are available at <https://catmaid.jekelylab.ex.ac.uk>. The dataset encompasses all EM images (in JPG format), skeletons, meshes, node tags, connectors, and annotations. Additionally, we provide all R scripts used for data acquisition and figure generation (Jokura et al., 2025). All plots, figures (including anatomical renderings), and figure layouts can be fully reproduced using the provided R scripts. While the scripts are mostly organized by figure, some general-purpose scripts—for tasks such as loading libraries, accessing CATMAID data, and defining common functions—are shared across multiple figures.

Acknowledgements

This work was supported by the Japan Society for the Promotion of Science (JSPS) Overseas Research Fellowships, the Grass Foundation, the Kavli Foundation, and the Marine Biological Laboratory (MBL). This project also received funding from the European Research Council (ERC) under the European Union's Horizon 2020 research and innovation programme (grant agreement No. 101020792). We thank Dr. Réza Shahidi for sectioning and imaging, Paulina Cherek for high-pressure freezing and sample preparation, and Iva Verbanac for help with tracing. We are also grateful to Dr. Chris Bjornsson, the MBL Central Microscopy Facility, Dr. Shoji A. Baba, and Dr. Kogiku Shiba for their assistance with microscopy. We also thank Dr. Sidney L. Tamm and Dr. Steven H. D. Haddock for their valuable feedback on the manuscript.

References

- Arendt D. 2021. Elementary nervous systems. *Philosophical Transactions of the Royal Society B: Biological Sciences* **376**:20200347. doi:[10.1098/rstb.2020.0347](https://doi.org/10.1098/rstb.2020.0347)
- Aronova M. 1974. Electron microscopic observation of the aboral organ of ctenophora. I. The gravity receptor. *Zeitschrift fur mikroskopisch-anatomische Forschung* **88**:401–412.
- Arshavsky Y. 2003. Cellular and network properties in the functioning of the nervous system: from central pattern generators to cognition. *Brain Research Reviews* **41**:229–267. doi:[10.1016/s0165-0173\(02\)00249-7](https://doi.org/10.1016/s0165-0173(02)00249-7)
- Bates AS, Manton JD, Jagannathan SR, Costa M, Schlegel P, Rohlfing T, Jefferis GS. 2020. The *natverse*, a versatile toolbox for combining and analysing neuroanatomical data. *eLife* **9**. doi:[10.7554/elife.53350](https://doi.org/10.7554/elife.53350)
- Burkhardt P, Colgren J, Medhus A, Digel L, Naumann B, Soto-Angel JJ, Nordmann E-L, Sachkova MY, Kittelmann M. 2023. Syncytial nerve net in a ctenophore adds insights on the evolution of nervous systems. *Science* **380**:293–297. doi:[10.1126/science.adc5645](https://doi.org/10.1126/science.adc5645)
- Burkhardt P, Jékely G. 2021. Evolution of synapses and neurotransmitter systems: The divide-and-conquer model for early neural cell-type evolution. *Current Opinion in Neurobiology* **71**:127–138. doi:[10.1016/j.conb.2021.11.002](https://doi.org/10.1016/j.conb.2021.11.002)
- Calderón LAB, Shahidi R, Jékely G. 2024. [Mechanism of barotaxis in marine zooplankton](#).
- Cardona A, Saalfeld S, Schindelin J, Arganda-Carreras I, Preibisch S, Longair M, Tomancak P, Hartenstein V, Douglas RJ. 2012. TrakEM2 Software for Neural Circuit Reconstruction. *PLoS ONE* **7**:e38011. doi:[10.1371/journal.pone.0038011](https://doi.org/10.1371/journal.pone.0038011)
- Colin SP, Costello JH, Hansson LJ, Titelman J, Dabiri JO. 2010. Stealth predation and the predatory success of the invasive ctenophore *Mnemiopsis leidyi*. *Proceedings of the National Academy of Sciences* **107**:17223–17227. doi:[10.1073/pnas.1003170107](https://doi.org/10.1073/pnas.1003170107)
- Courtney A, Merces GOT, Pickering M. 2020. [Characterising the behaviour of the ctenophore *Pleurobrachia pileus* in a laboratory aquaculture system](#).

- Ferraioli A, Digel L, Sturm D, Colgren J, Le Goff C, Jan A, Soto-Angel JJ, Naumann B, Kittelmann M, Burkhardt P. 2025. [The 3D architecture of the ctenophore aboral organ and the evolution of complex integrative centers in animals.](#)
- Hayakawa E, Guzman C, Horiguchi O, Kawano C, Shiraishi A, Mohri K, Lin M-F, Nakamura R, Nakamura R, Kawai E, Komoto S, Jokura K, Shiba K, Shigenobu S, Satake H, Inaba K, Watanabe H. 2022. Mass spectrometry of short peptides reveals common features of metazoan peptidergic neurons. *Nature Ecology & Evolution* **6**:1438–1448. doi:[10.1038/s41559-022-01835-7](https://doi.org/10.1038/s41559-022-01835-7)
- Hernandez-Nicase M-L. 1984. CtenophoraBiology of the Integument. Springer Berlin Heidelberg. pp. 96–111. doi:[10.1007/978-3-642-51593-4_9](https://doi.org/10.1007/978-3-642-51593-4_9)
- Hernandez-Nicase M-L. 1974. Ultrastructural evidence for a sensory-motor neuron in Ctenophora. *Tissue and Cell* **6**:43–47. doi:[10.1016/0040-8166\(74\)90021-4](https://doi.org/10.1016/0040-8166(74)90021-4)
- Hernandez-Nicase M-L. 1973. Le Système Nerveux des Cténaires. *Zeitschrift für Zellforschung und Mikroskopische Anatomie* **137**:223–250. doi:[10.1007/BF00307432](https://doi.org/10.1007/BF00307432)
- Hernandez-Nicase M-L. 1968. Specialized Connexions between Nerve Cells and Mesenchymal Cells in Ctenophores. *Nature* **217**:1075–1076. doi:[10.1038/2171075a0](https://doi.org/10.1038/2171075a0)
- Hertwig R. 1880. Ueber den bau der ctenophoren. *Jenaische Zeitschrift für Naturwissenschaft* **14**:393.
- Horridge GA. 1965. Relations between nerves and cilia in ctenophores. *American Zoologist* **5**:357–375. doi:[10.1093/icb/5.3.357](https://doi.org/10.1093/icb/5.3.357)
- Horridge GA, Mackay B. 1964. Neurociliary synapses in pleurobrachia (ctenophora). *Journal of Cell Science* **S3-105**:163–174. doi:[10.1242/jcs.s3-105.70.163](https://doi.org/10.1242/jcs.s3-105.70.163)
- Jager M, Chiori R, Alié A, Dayraud C, Quéinnec E, Manuel M. 2010. New insights on ctenophore neural anatomy: Immunofluorescence study in *Pleurobrachia pileus* (Müller, 1776). *Journal of Experimental Zoology Part B: Molecular and Developmental Evolution* **316B**:171–187. doi:[10.1002/jez.b.21386](https://doi.org/10.1002/jez.b.21386)
- Jékely G. 2010. Origin and early evolution of neural circuits for the control of ciliary locomotion. *Proceedings of the Royal Society B: Biological Sciences* **278**:914–922. doi:[10.1098/rspb.2010.2027](https://doi.org/10.1098/rspb.2010.2027)
- Jurisch-Yaksi N, Wachten D, Gopalakrishnan J. 2024. The neuronal cilium a highly diverse and dynamic organelle involved in sensory detection and neuromodulation. *Trends in Neurosciences* **47**:383–394. doi:[10.1016/j.tins.2024.03.004](https://doi.org/10.1016/j.tins.2024.03.004)
- Keijzer F, Duijn M van, Lyon P. 2013. What nervous systems do: early evolution, inputoutput, and the skin brain thesis. *Adaptive Behavior* **21**:67–85. doi:[10.1177/1059712312465330](https://doi.org/10.1177/1059712312465330)
- Kennedy A, Weissbourd B. 2024. Dynamics of neural activity in early nervous system evolution. *Current Opinion in Behavioral Sciences* **59**:101437. doi:[10.1016/j.cobeha.2024.101437](https://doi.org/10.1016/j.cobeha.2024.101437)
- Li Y, Shen X-X, Evans B, Dunn CW, Rokas A. 2021. Rooting the Animal Tree of Life. *Molecular Biology and Evolution* **38**:4322–4333. doi:[10.1093/molbev/msab170](https://doi.org/10.1093/molbev/msab170)
- Lowe B. 1997. The role of Ca²⁺ in deflection-induced excitation of motile, mechanoresponsive balancer cilia in the ctenophore statocyst. *Journal of experimental biology* **200**:1593–1606.
- Marinković M, Berger J, Jékely G. 2019. Neuronal coordination of motile cilia in locomotion and feeding. *Philosophical Transactions of the Royal Society B: Biological Sciences* **375**:20190165. doi:[10.1098/rstb.2019.0165](https://doi.org/10.1098/rstb.2019.0165)
- Martindale MQ, Henry JQ. 1999. Intracellular Fate Mapping in a Basal Metazoan, the Ctenophore *Mnemiopsis leidyi*, Reveals the Origins of Mesoderm and the Existence of Indeterminate Cell Lineages. *Developmental Biology* **214**:243–257. doi:[10.1006/dbio.1999.9427](https://doi.org/10.1006/dbio.1999.9427)
- Moroz LL. 2015. Convergent evolution of neural systems in ctenophores. *Journal of Experimental Biology* **218**:598–611. doi:[10.1242/jeb.110692](https://doi.org/10.1242/jeb.110692)
- Moroz LL, Kocot KM, Citarella MR, Dosung S, Norekian TP, Povolotskaya IS, Grigorenko AP, Dailey C, Berezikov E, Buckley KM, Ptitsyn A, Reshetov D, Mukherjee K, Moroz TP, Bobkova Y, Yu F, Kapitonov VV, Jurka J, Bobkov YV, Swore JJ, Girardo DO, Fodor A, Gusev F, Sanford R, Bruders R, Kittler E, Mills CE, Rast JP, Derelle R, Solovyev VV, Kondrashov FA, Swalla BJ, Sweedler JV, Rogaev EI, Halanych KM, Kohn AB. 2014. The ctenophore genome and the evolutionary origins of neural systems. *Nature* **510**:109–114. doi:[10.1038/nature13400](https://doi.org/10.1038/nature13400)
- Roberts RVJ, Pop S, Prieto-Godino LL. 2022. Evolution of central neural circuits: state of the art and perspectives. *Nature Reviews Neuroscience* **23**:725–743. doi:[10.1038/s41583-022-00644-y](https://doi.org/10.1038/s41583-022-00644-y)

- Ryan JF, Pang K, Schnitzler CE, Nguyen A-D, Moreland RT, Simmons DK, Koch BJ, Francis WR, Havlak P, Smith SA, Putnam NH, Haddock SHD, Dunn CW, Wolfsberg TG, Mullikin JC, Martindale MQ, Baxevanis AD. 2013. The Genome of the Ctenophore *Mnemiopsis leidyi* and Its Implications for Cell Type Evolution. *Science* **342**. doi:[10.1126/science.1242592](https://doi.org/10.1126/science.1242592)
- Saalfeld S, Cardona A, Hartenstein V, Tomančák P. 2009. CATMAID: collaborative annotation toolkit for massive amounts of image data. *Bioinformatics* **25**:1984–1986. doi:[10.1093/bioinformatics/btp266](https://doi.org/10.1093/bioinformatics/btp266)
- Sachkova MY, Nordmann E-L, Soto-Ángel JJ, Meeda Y, Górska B, Naumann B, Dondorp D, Chatzigeorgiou M, Kittelmann M, Burkhardt P. 2021. Neuropeptide repertoire and 3D anatomy of the ctenophore nervous system. *Current Biology* **31**:5274–5285.e6. doi:[10.1016/j.cub.2021.09.005](https://doi.org/10.1016/j.cub.2021.09.005)
- Schneider-Mizell CM, Gerhard S, Longair M, Kazimiers T, Li F, Zwart MF, Champion A, Midgley FM, Fetter RD, Saalfeld S, Cardona A. 2016. Quantitative neuroanatomy for connectomics in *Drosophila*. *eLife* **5**. doi:[10.7554/elife.12059](https://doi.org/10.7554/elife.12059)
- Schultz DT, Haddock SHD, Bredeson JV, Green RE, Simakov O, Rokhsar DS. 2023. Ancient gene linkages support ctenophores as sister to other animals. *Nature* **618**:110–117. doi:[10.1038/s41586-023-05936-6](https://doi.org/10.1038/s41586-023-05936-6)
- Sebé-Pedrós A, Chomsky E, Pang K, Lara-Astiaso D, Gaiti F, Mukamel Z, Amit I, Hejnol A, Degnan BM, Tanay A. 2018. Early metazoan cell type diversity and the evolution of multicellular gene regulation. *Nature Ecology & Evolution* **2**:1176–1188. doi:[10.1038/s41559-018-0575-6](https://doi.org/10.1038/s41559-018-0575-6)
- Selverston AI. 2010. Invertebrate central pattern generator circuits. *Philosophical Transactions of the Royal Society B: Biological Sciences* **365**:2329–2345. doi:[10.1098/rstb.2009.0270](https://doi.org/10.1098/rstb.2009.0270)
- Sheu S-H, Upadhyayula S, Dupuy V, Pang S, Deng F, Wan J, Walpita D, Pasolli HA, Houser J, Sanchez-Martinez S, Brauchi SE, Banala S, Freeman M, Xu CS, Kirchhausen T, Hess HF, Lavis L, Li Y, Chaumont-Dubel S, Clapham DE. 2022. A serotonergic axon-cilium synapse drives nuclear signaling to alter chromatin accessibility. *Cell* **185**:3390–3407.e18. doi:[10.1016/j.cell.2022.07.026](https://doi.org/10.1016/j.cell.2022.07.026)
- Stanley GD, Stürmer W. 1983. The first fossil ctenophore from the Lower Devonian of West Germany. *Nature* **303**:518–520. doi:[10.1038/303518a0](https://doi.org/10.1038/303518a0)
- Tamm S. 1982. Electrical conduction and behaviour in "simple" invertebrates. (*No Title*).
- Tamm S. 1980. Cilia and ctenophores. *Oceanus* **23**:50–59.
- Tamm SL. 2015. Functional Consequences of the Asymmetric Architecture of the Ctenophore Statocyst. *The Biological Bulletin* **229**:173–184. doi:[10.1086/bblv229n2p173](https://doi.org/10.1086/bblv229n2p173)
- Tamm SL. 2014a. Formation of the statolith in the ctenophore *mnemiopsis leidyi*. *The Biological Bulletin* **227**:7–18. doi:[10.1086/bblv227n1p7](https://doi.org/10.1086/bblv227n1p7)
- Tamm SL. 2014b. Cilia and the life of ctenophores. *Invertebrate Biology* **133**:1–46. doi:[10.1111/ivb.12042](https://doi.org/10.1111/ivb.12042)
- Tamm SL, Tamm S. 2002. Novel bridge of axon-like processes of epithelial cells in the aboral sense organ of ctenophores. *Journal of Morphology* **254**:99–120. doi:[10.1002/jmor.10019](https://doi.org/10.1002/jmor.10019)
- Verasztó C, Ueda N, Bezires-Calderón LA, Panzera A, Williams EA, Shahidi R, Jékely G. 2017. Ciliomotor circuitry underlying whole-body coordination of ciliary activity in the *Platynereis* larva. *eLife* **6**. doi:[10.7554/elife.26000](https://doi.org/10.7554/elife.26000)
- Waggett R. 1999. Capture mechanisms used by the lobate ctenophore, *mnemiopsis leidyi*, preying on the copepod acartia tonsa. *Journal of Plankton Research* **21**:2037–2052. doi:[10.1093/plankt/21.11.2037](https://doi.org/10.1093/plankt/21.11.2037)
- Whelan NV, Kocot KM, Moroz LL, Halanych KM. 2015. Error, signal, and the placement of Ctenophora sister to all other animals. *Proceedings of the National Academy of Sciences* **112**:5773–5778. doi:[10.1073/pnas.1503453112](https://doi.org/10.1073/pnas.1503453112)
- Wiljes OO de, Elburg RAJ van, Biehl M, Keijzer FA. 2015. Modeling spontaneous activity across an excitable epithelium: Support for a coordination scenario of early neural evolution. *Frontiers in Computational Neuroscience* **9**. doi:[10.3389/fncom.2015.00110](https://doi.org/10.3389/fncom.2015.00110)

Supplementary material

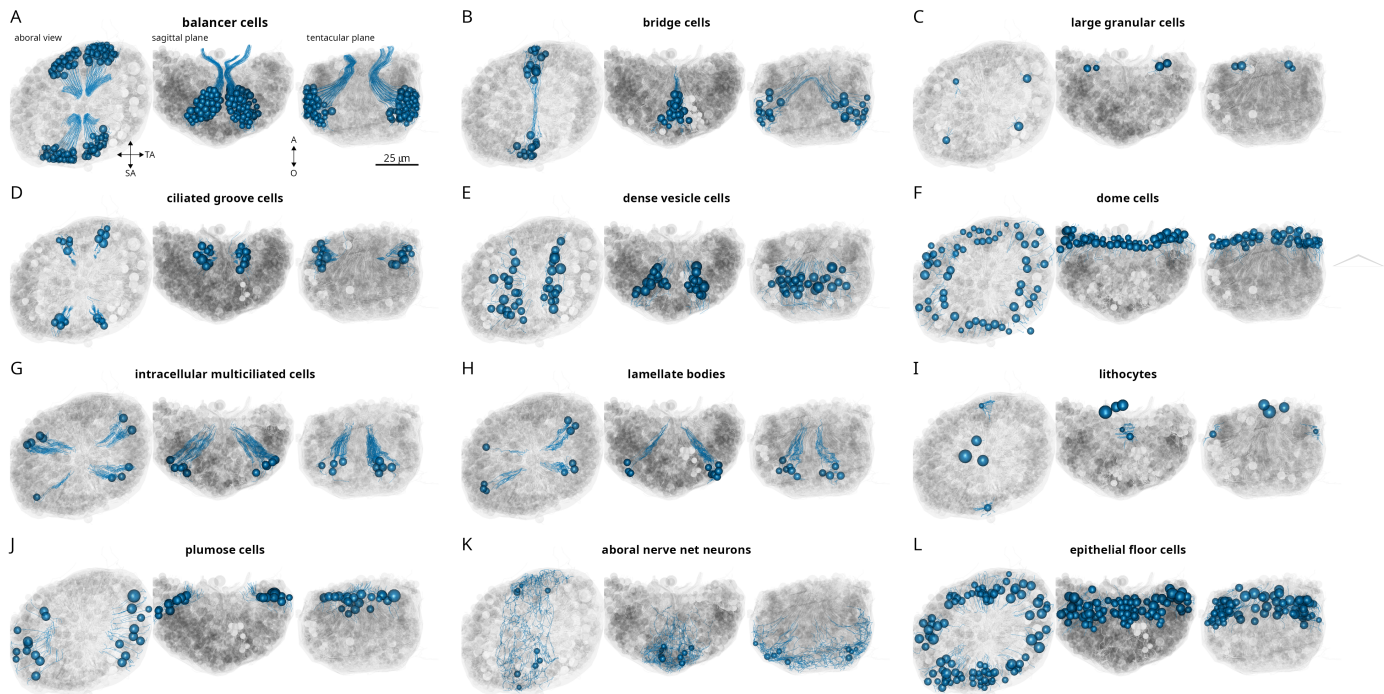


Figure 1—figure supplement 1. Cell-type composition of the ctenophore aboral organ

Morphological rendering of skeletonised cell types, (A) balancer cells (B) bridge cells, (C) large granular cells, (D) ciliated groove cells, (E) dense vesicle cells, (F) dome cells, (G) intra-multiciliated cells, (H) lamellate bodies, (I) lithocytes, (J) plumose cells, (K) aboral nerve-net neurons (L) epithelial floor cells.

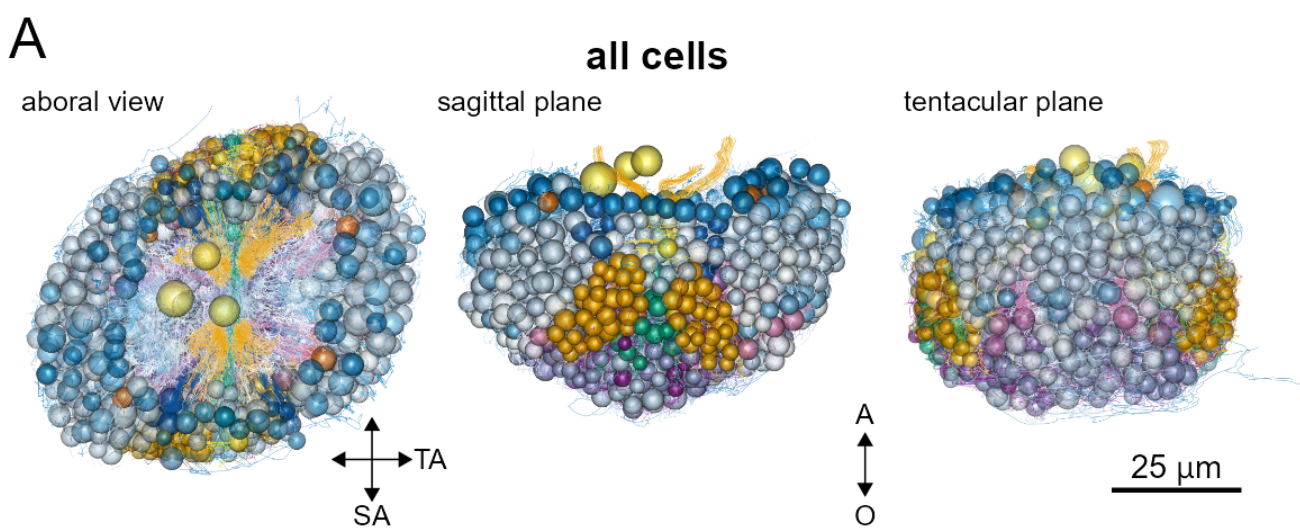


Figure 1—figure supplement 2. 3D reconstruction of all cells comprising the aboral organ

(A) Morphological rendering of skeletonised cells in the ctenophore aboral organ. Each color represents a distinct cell type. The balancer cells are shown in orange. Some cell groups lack distinguishing subcellular features required for identification and are shown in white.

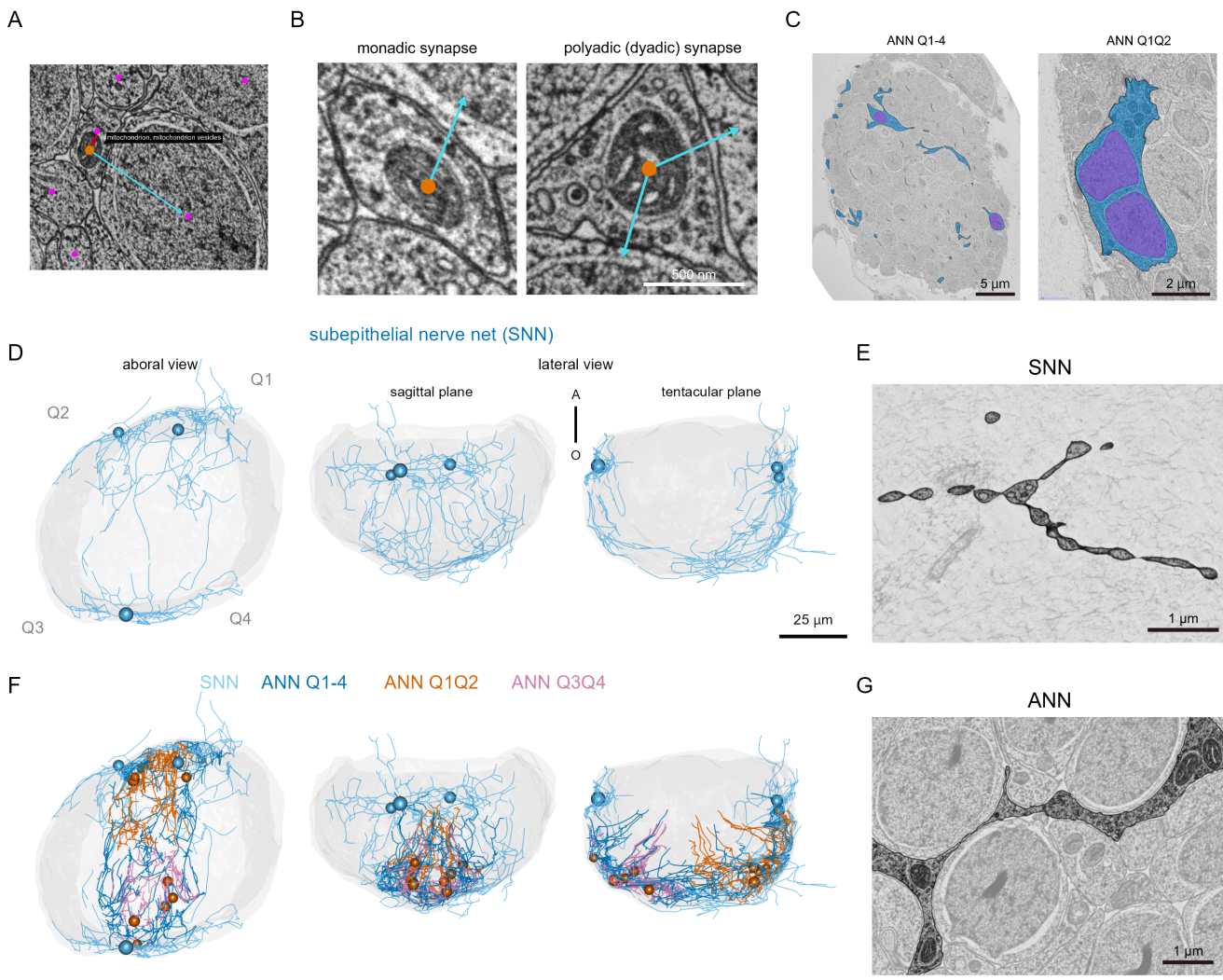


Figure 2—figure supplement 1. Ultrastructural features and synaptic organization of the ANN, in comparison to the subepithelial nerve net (SNN)

(A) Registration and annotation of synapses in the actual cellular traces. Pink dots indicate the approximate center of each individual cell, marked within its plasma membrane boundary. Mitochondria involved in synaptic contacts are labeled with orange dots. Red arrows point from these mitochondria to the presynaptic cell body, marking presynaptic structures. Cyan arrows point from the orange-labeled mitochondria to the corresponding postsynaptic cell.

(B) Electron microscopy (EM) images showing representative presynaptic structures. The left panel shows a monadic synapse, while the right panel shows a polyadic (dyadic) synapse, in which a single presynaptic site contacts two postsynaptic cells.

(C) Nuclei within two different types of ANN cells are shown in purple in a single EM section. On the left, the ANN_Q1-4 cell extends widely across the aboral organ and appears as a continuous structure in 3D, despite having nuclei located distantly from each other. In contrast, ANN_Q1Q2 (right) has two adjacent nuclei.

(D) Three-dimensional reconstruction of the subepithelial nerve net (SNN). The SNN extends broadly, enveloping the aboral organ. Some portions of the network remain as unconnected fragments due to incomplete reconstruction.

(E) Morphological comparison between the ANN in EM images. The SNN shows a “beads-on-a-string” morphology, with discrete bead-like swellings connected by faint electron-dense fibrous structures.

(F) Three-dimensional reconstruction of the SNN and ANNs.

(G) Morphological comparison between the SNN in EM images. The ANN exhibits a more diffuse distribution, often appearing to interdigitate between surrounding cells. Relatively large mitochondria are frequently observed in the ANN processes.

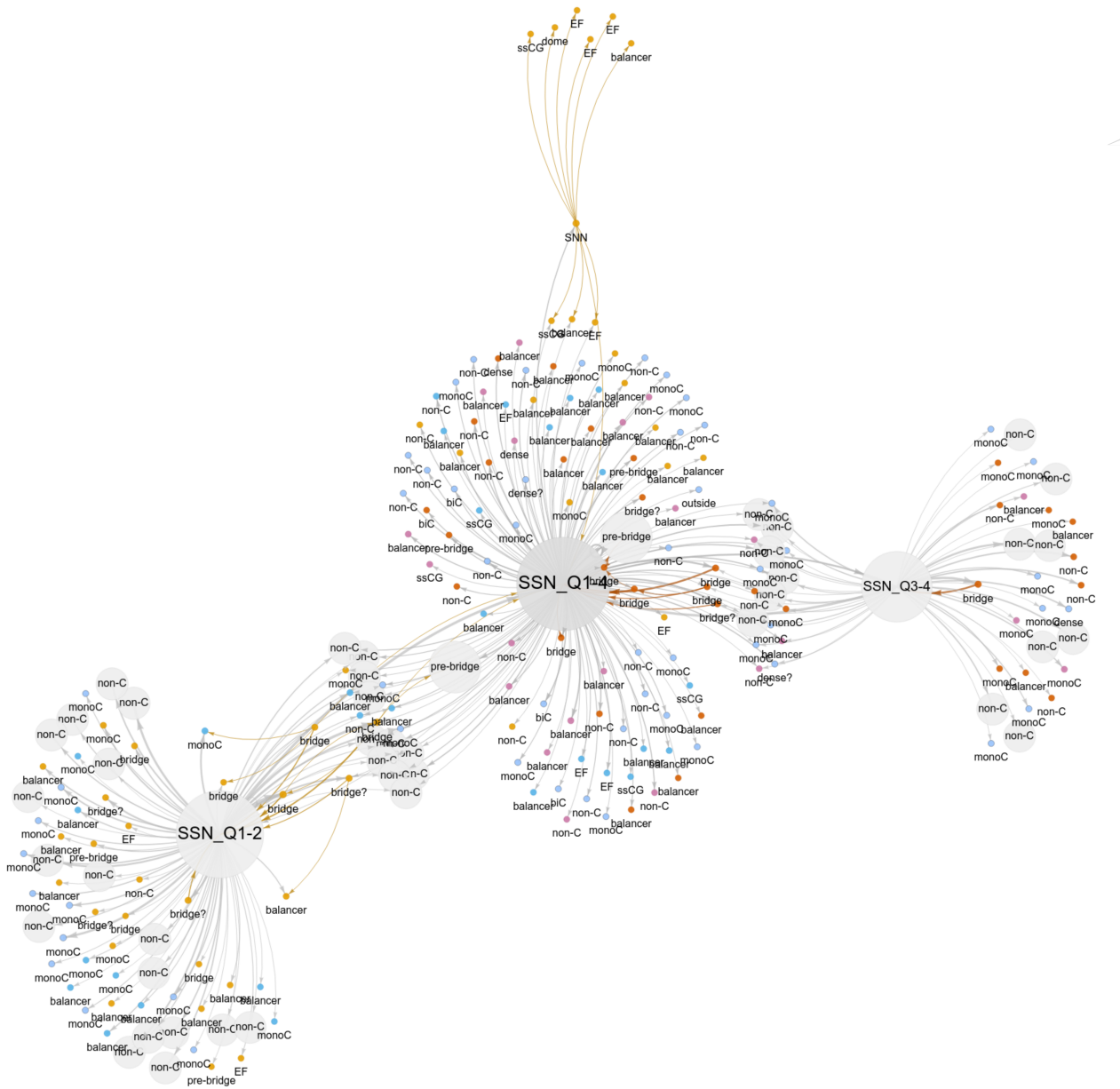


Figure 3—figure supplement 1. Full synaptic connectome of the ctenophore apical organ

Full synaptic graph showing individual cells as nodes connected by synaptic contacts. Arrows point from the presynaptic to the postsynaptic cell. Edge thickness is proportional to the number of synapses.

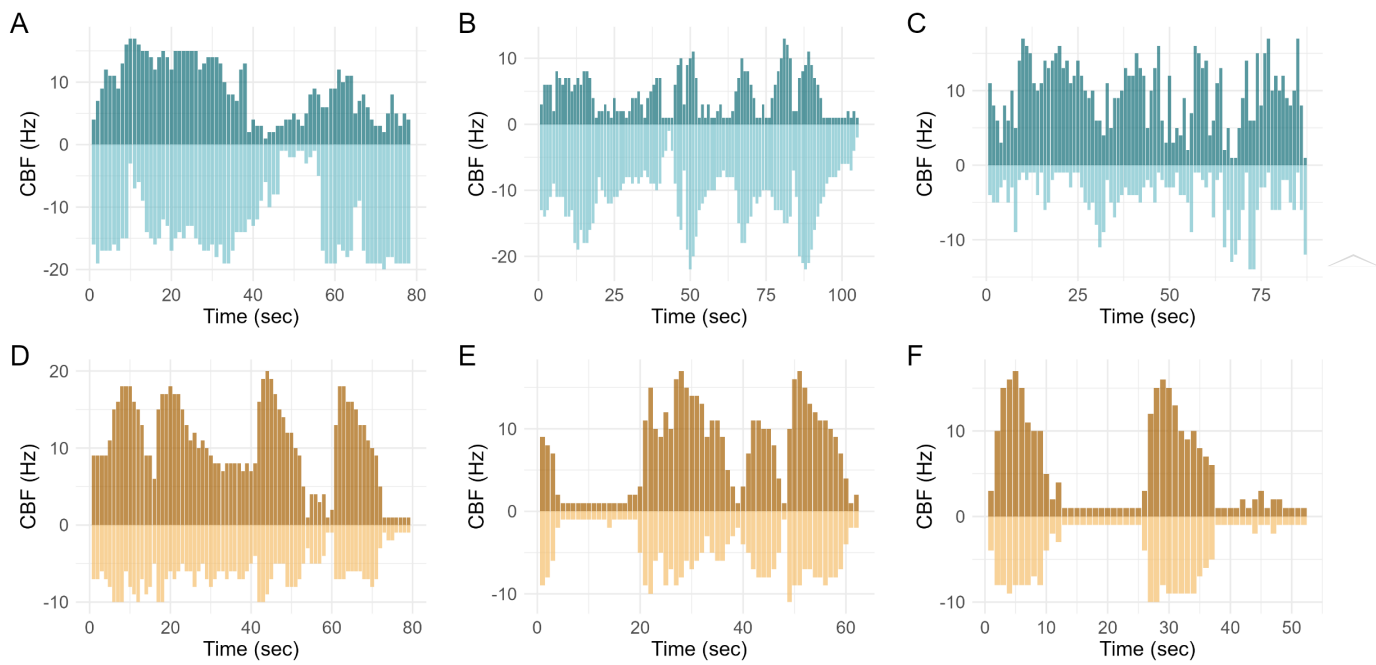


Figure 4—figure supplement 1. Ciliary beat frequency (CBF) dynamics of balancer cells in additional samples

Bar plots showing CBF dynamics of left and right balancers (top and bottom panels, respectively) recorded from the sagittal (A–C) and tentacular (D–F) planes. Positive and negative values indicate opposing sides within each imaging plane. These data correspond to additional samples not shown in the main figure and support the results presented in Figure 4E.

Video 1. Morphological rendering of the aboral organ, featuring three distinct cell types—balancer cells, bridge cells, and components of the apical nerve net (ANN). Cells of each type are subdivided and color-coded according to their spatial regions. A lithocyte is shown in gray as a reference point, and the outline of the aboral organ is indicated in white.

Video 2. Visualization of balancer cilia extending from basal bodies, marked by red dots. Each red dot indicates the position of a basal body, from which the cilium projects distally. A lithocyte is shown in gray as a reference point, and the outline of the aboral organ is indicated in white.

Video 3. High-speed imaging of balancer ciliary beating along with kymographs from two individual balancer ciliary bundles. The recording was acquired at 100 frames per second and played back at 30 frames per second (0.3×). The white line overlaid on the kymographs indicates the current time point shown in the video. This example captures a ciliary arrest event in the sagittal plane.

Video 4. High-speed imaging of balancer ciliary beating along with kymographs from two individual balancer ciliary bundles. The recording was acquired at 100 frames per second and played back at 30 frames per second (0.3×). The white line overlaid on the kymographs indicates the current time point shown in the video. This example captures a ciliary re-beat event in the sagittal plane.

Video 5. High-speed imaging of balancer ciliary beating along with kymographs from two individual balancer ciliary clusters. The recording was acquired at 100 frames per second and played back at 30 frames per second (0.3×). The white line overlaid on the kymographs indicates the current time point shown in the video. This example captures a ciliary arrest event in the tentacular plane.

Video 6. High-speed imaging of balancer ciliary beating along with kymographs from two individual balancer ciliary clusters. The recording was acquired at 100 frames per second and played back at 30 frames per second (0.3×). The white line overlaid on the kymographs indicates the current time point shown in the video. This example captures a ciliary re-beat event in the tentacular plane.

Video 7. High-speed imaging of balancer ciliary beating in the aboral organ tilted relative to gravity, illustrating gravity-induced asymmetry. The example on the left shows an aboral organ tilted by approximately 135° in the sagittal plane, while the example on the right shows one tilted by

approximately 60° in the tentacular plane. For each case, the left and right balancer ciliary clusters are displayed separately. Ciliary beating is shown alongside kymographs extracted from two representative clusters. Recordings were acquired at 100 frames per second and are played back at 30 frames per second (0.3×). A white vertical line overlaid on each kymograph indicates the current frame shown in the video. These examples demonstrate asymmetrical balancer activity consistent with geotactic responses reported by Tamm (1980) ([Tamm, 1980](#)).

